Wave-equation migration velocity analysis for anisotropic models on 2-D ExxonMobil field data

Yunyue (Elita) Li

ABSTRACT

I apply an anisotropic wave-equation migration velocity analysis (WEMVA) method on a 2-D ExxonMobil dataset. I start from the best anisotropic model available from seismic, walkaway VSPs and check shots. The initial gathers in the subsurface offset domain are already fairly well focused; however, after inversion using our WEMVA method, I obtain an image with better continuity and clearer faults. By looking at the angle gathers, it is easy to distinguish the contribution of the improved η model from the contribution of the velocity model.

INTRODUCTION

Compared with isotropic models, anisotropic models are recognized as more realistic representations of the subsurface in complex geological environment. These models are better defined and verified in developing and production areas. However, anisotropic parameters cannot be fully constrained by surface seismic data. Therefore, anisotropic models are better defined in well-developed and production areas, where various well log, check shots and VSP data are available. The ExxonMobil dataset used in this study is from a producing area in an offshore sedimentary basin close to a huge salt body. Figure 1 illustrates the available datasets in this area. While vertical check shots and sonic logs best constrain the vertical velocity model, offset check shot (OCS) data, thanks to its long offset give information on both vertical and horizontal velocity . The current anisotropic model is built using an interactive visualization method (Bear et al., 2005) that integrates surface seismic, sonic logs, vertical check shots, and offset check shots.

From the results shown in Figure 2, we can see that the anisotropic prestack depth migration (APSDM) gathers are almost flat, inverted velocities have a reasonable match with the sonic logs, and the modeled traveltime agrees with the offset checkshot measurements. However, this interactive visualization method requires human inputs and corrections, which can be cumbersome when large-scale 3-D field data is under examination. Moreover, the most informative data - offset checkshot data - are only acquired sparsely in the 3-D domain, primarily around the salt body. Hence interpolation / extrapolation from these OCS locations is still needed to build a 3-D model elsewhere. This process may lead to inaccurate anisotropic models. Finally, according to the color code in Figure 1, although most of the traveltimes are fitted very

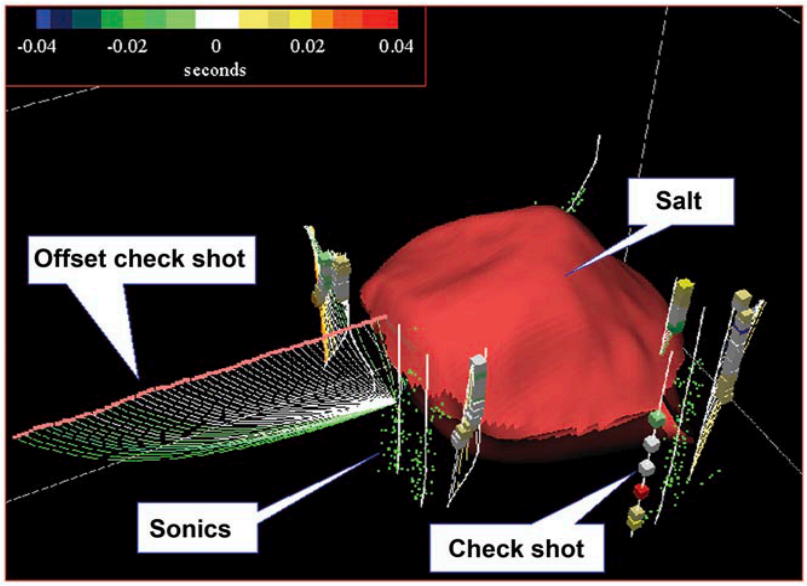

Figure 1: Available datasets for anisotropic model building. From Bear et al. (2005). The current anisotropic model is built using an interactive visualization method that integrates surface seismic, sonic logs, vertical check shots, and offset check shots. The green ray paths show a slower estimation of the velocity and/or a smaller estimation of η. [**NR**]

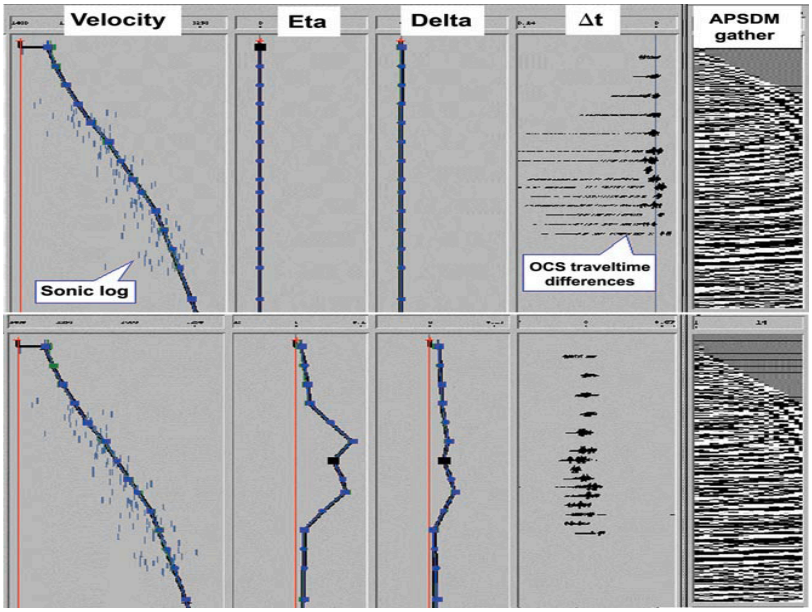

Figure 2: Visualization of interactive modeling for anisotropy. Top row: Initial isotropic model compared with sonic log and OCS traveltime. APSDM gather is already fairly flat in the small angles. Bottom row: Improved anisotropic model compared with sonic log and OCS traveltime. APSDM gathers are further flattened for large angles. From Bear et al. (2005). [**NR**]

well for near- to mid-offset check shots (indicated by rays in white), the travel times modeled between long-offset shots and the downhole receivers are still underestimated compared with the measured travel times (indicated by rays in green). Therefore, a fully automated anisotropic model building method utilizing all types of data would be highly valuable to improve the current model.

To test our method of anisotropic WEMVA (Li and Biondi, 2011), we take a 2-D slice through the sediment basin from this 3-D field dataset where the salt body is far away. The inversion is initialized by the current best model. After 8 iterations, we obtain updated velocity and η model that better define the faults in this section and have better continuities in some reflectors.

THEORY

Unlike in the previous paper (Li and Biondi, 2011), we derive the anisotropic WEMVA gradients using a Lagrangian augmented functional instead of perturbation theory. The derivation is hence neat and straightforward, and the interpretations of the adjoint-state equations suggest the same implementation as perturbation theory suggests.

We parameterize the VTI subsurface using NMO slowness s_n, and Thomson parameters η and δ (Thomsen, 1986). In the shot-profile domain, both source wavefields $\mathbf{D}$ and receiver wavefields $\mathbf{U}$ are downward continued using the following one-way wave equation and boundary condition (Shan, 2009):

$$\begin{cases} \left(\frac{1}{\sqrt{1+2\delta}}\frac{\partial}{\partial z} + i\Lambda\right) D(\mathbf{x},\mathbf{x}_s) = 0 \\ D(x,y,z=0,\mathbf{x}_s) = f_s\delta(\mathbf{x}-\mathbf{x}_s) \end{cases}, \tag{1}$$

and

$$\begin{cases} \left(\frac{1}{\sqrt{1+2\delta}}\frac{\partial}{\partial z} - i\Lambda\right) U(\mathbf{x},\mathbf{x}_s) = 0 \\ U(x,y,z=0,\mathbf{x}_s) = Q(x,y,z=0,\mathbf{x}_s) \end{cases}, \tag{2}$$

where

$$\Lambda = \omega s_n \sqrt{1 - \frac{|\mathbf{k}|^2}{\omega^2 s_n^2 - 2\eta|\mathbf{k}|^2}}. \tag{3}$$

Equations 1 and 2 can be summarized in matrix forms as follows:

$$\mathbf{L}\mathbf{D} = \mathbf{f} \tag{4}$$

and

$$\mathbf{L}^*\mathbf{U} = \mathbf{d}, \tag{5}$$

where

$$\mathbf{f} = f_s\delta(\mathbf{x}-\mathbf{x}_s, z), \tag{6}$$

$$\mathbf{d} = d_{\mathbf{x}_s}\delta(\mathbf{x} - \mathbf{x}_r, z), \tag{7}$$

and

$$\mathbf{L} = \frac{1}{\sqrt{1+2\delta}}\frac{\partial}{\partial z} - i\Lambda. \tag{8}$$

It is well known that parameter δ is the least constrained by surface seismic data because of the lack of depth information. Therefore, we assume δ can be correctly obtained from other sources of information, such as check shots and well logs. In this paper, we are going to invert for NMO slowness s_n and η.

We use an extended imaging condition (Sava and Formel, 2006) to compute the image cube with subsurface offsets:

$$I_{\mathbf{h}} = (\mathbf{S}_{+\mathbf{h}}\mathbf{p})^*(\mathbf{S}_{-\mathbf{h}}\mathbf{q}), \tag{9}$$

where $\mathbf{S}_{+\mathbf{h}}$ is a shifting operator which shifts the wavefield $+\mathbf{h}$ in the $\mathbf{x}$ direction. Notice that $(\mathbf{S}_{+\mathbf{h}})^* = \mathbf{S}_{-\mathbf{h}}$. Equations 4, 5 and 9 are state equations, and $\mathbf{D}$, $\mathbf{U}$ and $I_{\mathbf{h}}$ are the state variables.

To evaluate the accuracy of the subsurface model, we use a DSO objective function (Shen, 2004):

$$J = \frac{1}{2}\sum_{\mathbf{h}}\langle \mathbf{h}I_{\mathbf{h}}, \mathbf{h}I_{\mathbf{h}}\rangle. \tag{10}$$

where $\mathbf{h}$ is the subsurface offset. In practice, other objective functions (linear transformations of the image) can be used rather than DSO. To derive the DSO objective function with respect to s_n and η, we follow the recipe provided by Plessix (2006). First, we form the Lagrangian augmented functional:

$$\begin{aligned}\mathcal{L}(\mathbf{D}, \mathbf{U}, I_{\mathbf{h}}; \lambda, \mu, \gamma_{\mathbf{h}}; s_n, \epsilon) = & \qquad (11)\\ & \frac{1}{2}\sum_{\mathbf{h}}\langle \mathbf{h}\ I_{\mathbf{h}},\ \mathbf{h}\ I_{\mathbf{h}}\rangle \\ & + \langle \lambda,\ \mathbf{f} - \mathbf{L}(\mathbf{s_n}, \epsilon)\mathbf{D}\rangle \\ & + \langle \mu,\ \mathbf{d} - \mathbf{L}^*(\mathbf{s_n}, \epsilon)\mathbf{U}\rangle \\ & + \sum_{\mathbf{h}}\langle \gamma_{\mathbf{h}},\ (\mathbf{S}_{+\mathbf{h}}\mathbf{D})^*(\mathbf{S}_{-\mathbf{h}}\mathbf{U}) - I_{\mathbf{h}}\rangle\,. \qquad (12)\end{aligned}$$

Then the adjoint-state equations are obtained by taking the derivative of $\mathcal{L}$ with respect to state variables $\mathbf{D}$, $\mathbf{U}$ and $I_{\mathbf{h}}$:

$$\frac{\partial \mathcal{L}}{\partial \mathbf{D}} = -\mathbf{L}^*(s_n, \epsilon)\lambda + \sum_{\mathbf{h}}(\mathbf{S}_{+\mathbf{h}})^*(\mathbf{S}_{-\mathbf{h}}\mathbf{U})\gamma_{\mathbf{h}} = \mathbf{0}, \tag{13}$$

$$\frac{\partial \mathcal{L}}{\partial \mathbf{U}} = -\mathbf{L}(s_n, \epsilon)\mu + \sum_{\mathbf{h}}(\mathbf{S}_{-\mathbf{h}})^*(\mathbf{S}_{+\mathbf{h}}\mathbf{D})\gamma_{\mathbf{h}} = \mathbf{0}, \tag{14}$$

$$\frac{\partial \mathcal{L}}{\partial I_{\mathbf{h}}} = -\gamma_{\mathbf{h}} + \mathbf{h}^2 I_{\mathbf{h}} = 0, \forall\ \mathbf{h}. \tag{15}$$

Equation 13, 14, and 15 are the adjoint-state equations. Parameters λ, μ and $\gamma_{\mathbf{h}}$ are the adjoint-state variables, and can be calculated from the adjoint-state equations.

The physical interpretation of the adjoint-state equations offers better understanding of the physical process and provides insights for implementation. Clearly, the solution to equation 15, $\gamma_{\mathbf{h}}$, is the perturbed (residual) image at a certain subsurface offset. Equations 13 and 14 define the perturbed source and receiver wavefields, respectively. Notice the perturbed source wavefield λ at location $\mathbf{x}$ depends on the image at $(\mathbf{x}-\mathbf{h}, \mathbf{h})$ and the background receiver wavefield $\mathbf{U}$ at $\mathbf{x}-2\mathbf{h}$. The same rule applies to the perturbed receiver wavefield μ.

With the solutions to the equations above, we can now derive the gradients of the objective function 10 by taking the derivative of the augmented functional $\mathcal{L}$ with respect to the model variables s_n and ϵ as follows:

$$\nabla_{s_n} J \ = \ \left\langle \lambda,\ -\frac{\partial \mathbf{L}}{\partial \mathbf{s_n}}\mathbf{D} \right\rangle + \left\langle \mu,\ -\frac{\partial \mathbf{L}^*}{\partial \mathbf{s_n}}\mathbf{U} \right\rangle \tag{16}$$

$$\nabla_{\epsilon} J \ = \ \left\langle \lambda,\ -\frac{\partial \mathbf{L}}{\partial \epsilon}\mathbf{D} \right\rangle + \left\langle \mu,\ -\frac{\partial \mathbf{L}^*}{\partial \epsilon}\mathbf{U} \right\rangle. \tag{17}$$

It is straightforward to understand that the gradients for the model parameters are the crosscorrelations of the perturbed source / receiver wavefield and the scattered background receiver / source wavefield.

FIELD DATA TESTS

We extract a 2-D line from ExxonMobil dataset where the salt body is far away. Source spacing is 100 m, and receiver spacing is 50 m. The maximum offset in this 2-D line is about 4 km. This surface seismic dataset was acquired more than a decade ago; therefore the limited offsets of this dataset are insufficient from enough to constrain the anisotropic parameters. Fortunately, this area has been studied extensively by various types of other acquisitions: vertical check shots, offset check shots, and sonic logs. Therefore, a very well-defined anisotropic model is obtained from previous studies. We migrated the 2-D line using the anisotropic model provided (Figure 4(a) and Figure 4(b)). The initial stack image is shown on the top panel in Figure 6. Although the apparent dip is high due to the large vertical stretch (3 km in depth vs. 16 km on the horizontal axis), the reflectors in this 2-D line are pretty flat. We then estimate the dip field (Figure 3) from the initial image and use it to regularize the gradient for both velocity and η.

We can see many small-scale faults in this area on the top panel in Figure 6. Migration artifacts at $x = 13$ km and $z = 2500$ m are caused by a big vertical fault

running from $x = 14$ km on the top to the bottom of the section. The initial angle gathers are shown in the bottom row in Figure 6. Since this is a streamer geometry, the subsurface reflectors are only illuminated from positive angles. Although the gathers are almost flat, we can still see upward residual moveouts in the angle domain. Therefore, we have a chance to improve the model and the image by flattening the gathers.

Updates between the initial and the inverted velocity and η models are shown in Figure 5(a) and Figure 5(b), respectively. First, notice the spatial correlation between velocity updates and η updates, although no such constraints are applied during the inversion. However collocated, the update directions in velocity and η are not necessarily the same. We are able to resolve a localized shallow anomaly between 13 km and 15 km at around 800 m below surface. Comparing the initial stack image on the top panel in Figure 6 with the final stack image on the top panel of Figure 7, we can see improved continuity and signal strength in the area highlighted by the oval. The fault in this area is also better defined in the final image. Notice that the updates in velocity are less than 10%, whereas the updates in η are around 25%. These positive updates in both velocity and η agree well with the negative travel time misfits in the previous OCS modeling results (Figure 1).

We can also verify the updates in velocity and η on the angle gathers at different CMP locations. The initial angle domain common image gathers (ADCIGs) are shown in the bottom row in Figure 6, and the final ADCIGs produced using the inverted models are shown in the bottom row in Figure 7. To better illustrate the effects of the model updates, the ADCIGs are sampled more densely between CMP = 13 and 16 and sparsely outside of this range. In general, we can see improved flatness for all the reflectors. Specifically, for the shallower events above 1 km, most improvements happen at large angles over 35°. Therefore, we interpret the improvements for the shallow events primarily as the contribution of the improved η model.

For the deeper events at the same CMP location, both the depth and the flatness of the angle gather have been changed by inversion. The upward-curving events in the angle domain from the initial migration has been flattened by the improved velocity and η model. This result would be more convincing if we had the corresponding well logs at the same location to verify the depth shifts.

CONCLUSIONS AND FUTURE WORK

In this paper, we apply our anisotropic WEMVA algorithm to a 2-D slice of an ExxonMobil field dataset. The previous anisotropic model was built using all available datasets in the area: surface seismic, vertical and offset check shots and sonic logs. From the initial migrated image using the initial model, we observe upward moveout at large angles in the angle CIGs, which is consistent with the negative travel time misfits in the large-offset check shots. After 8 iterations of our non-linear anisotropic WEMVA iterations, we obtain a better subsurface image with flatter angle gathers

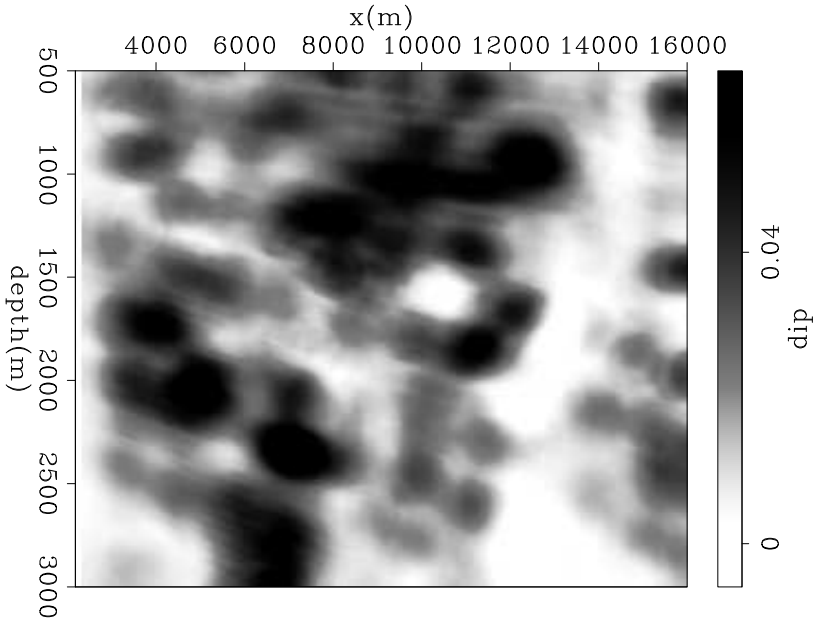

Figure 3: Estimated dip field from the initial image on the top panel of Figure 6. [**CR**]

and higher angle coverage.

The provided anisotropic model shows high spatial correlation between vertical velocity and Thomson parameters. Figure 8 shows a cross-plot among the parameters v_v, δ and η down to 1 km. The scatter plot shows distinct differences on different sides of the fault. Assuming these differences are based on the local geology and lithology, we should include this information into our model-building process in future work, possibly as a preconditioning constraint suggested by Li et al. (2011).

ACKNOWLEDGEMENT

The author thanks ExxonMobil for the permission to publish the field data example.

REFERENCES

Bear, L., T. Dickens, J. Krebs, J. Liu, and P. Traynin, 2005, Integrated velocity model estimation for improved positioning with anisotropic PSDM: The Leading Edge, 622–634.

Li, Y. and B. Biondi, 2011, Migration velocity analysis for anisotropic models: SEG Expanded Abstract, **30**, 201–206.

Li, Y., D. Nichols, K. Osypov, and R. Bachrach, 2011, Anisotropic tomography using rock physics contraints: 73^{rd} EAGE Conference & Exhibition.

Plessix, R.-E., 2006, A review of the adjoint-state method for computing the gradient of a funtional with geophysical applications: Geophysical Journal International, **167**, 495–503.

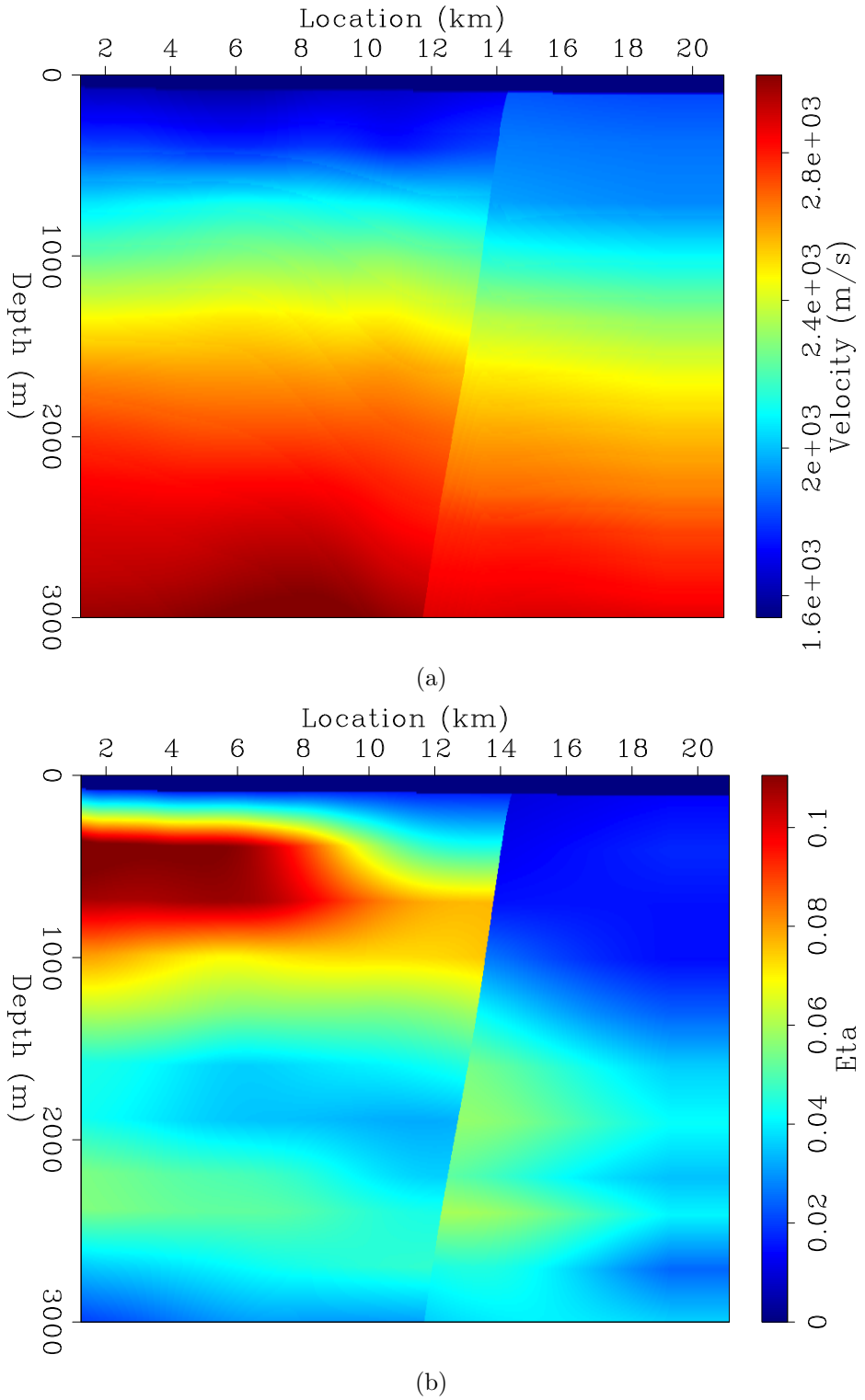

Figure 4: Initial velocity model (a) and initial η model (b). [**CR**]

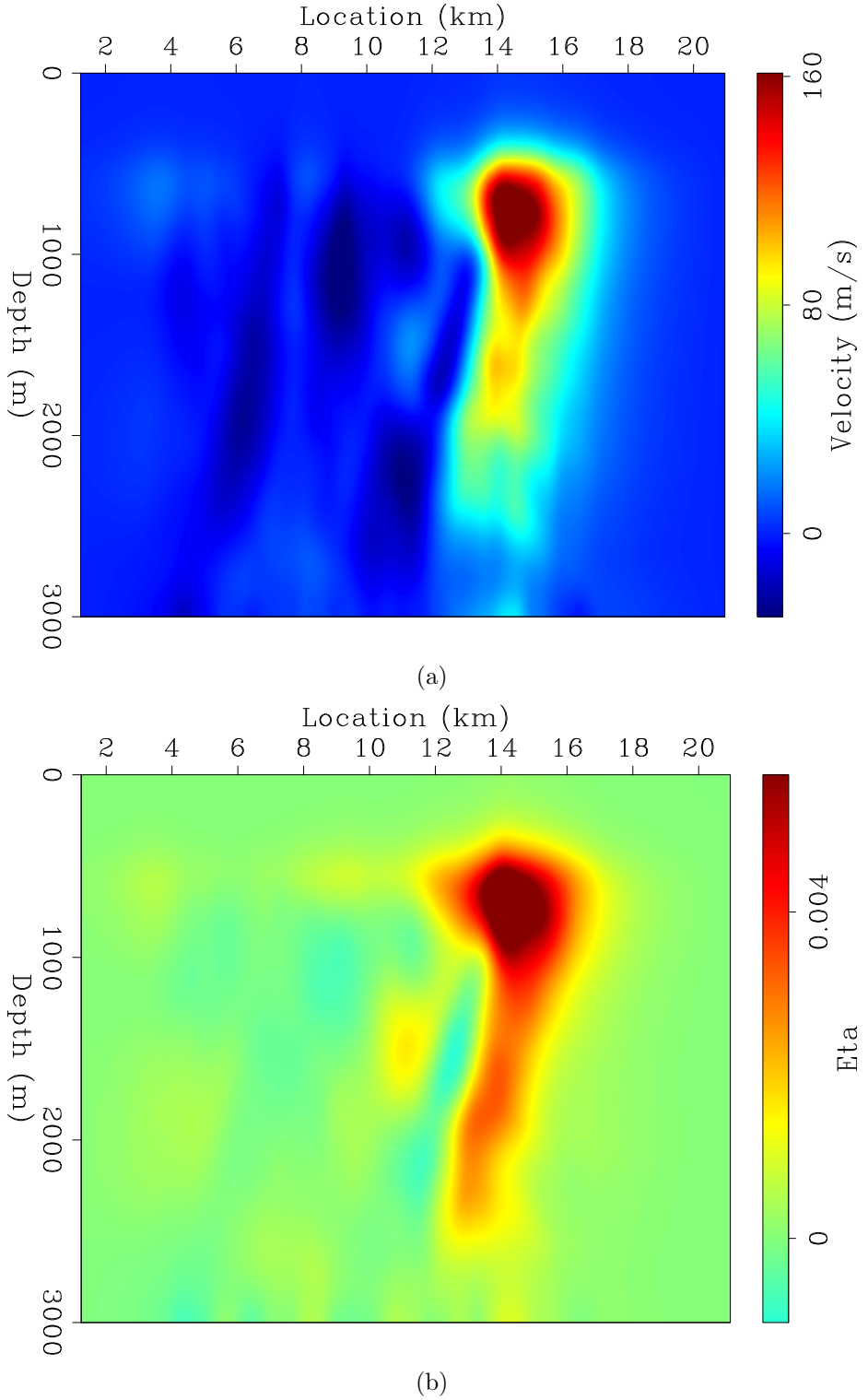

Figure 5: Updates in velocity model (a) and updates in η model (b) after inversion. [**CR**]

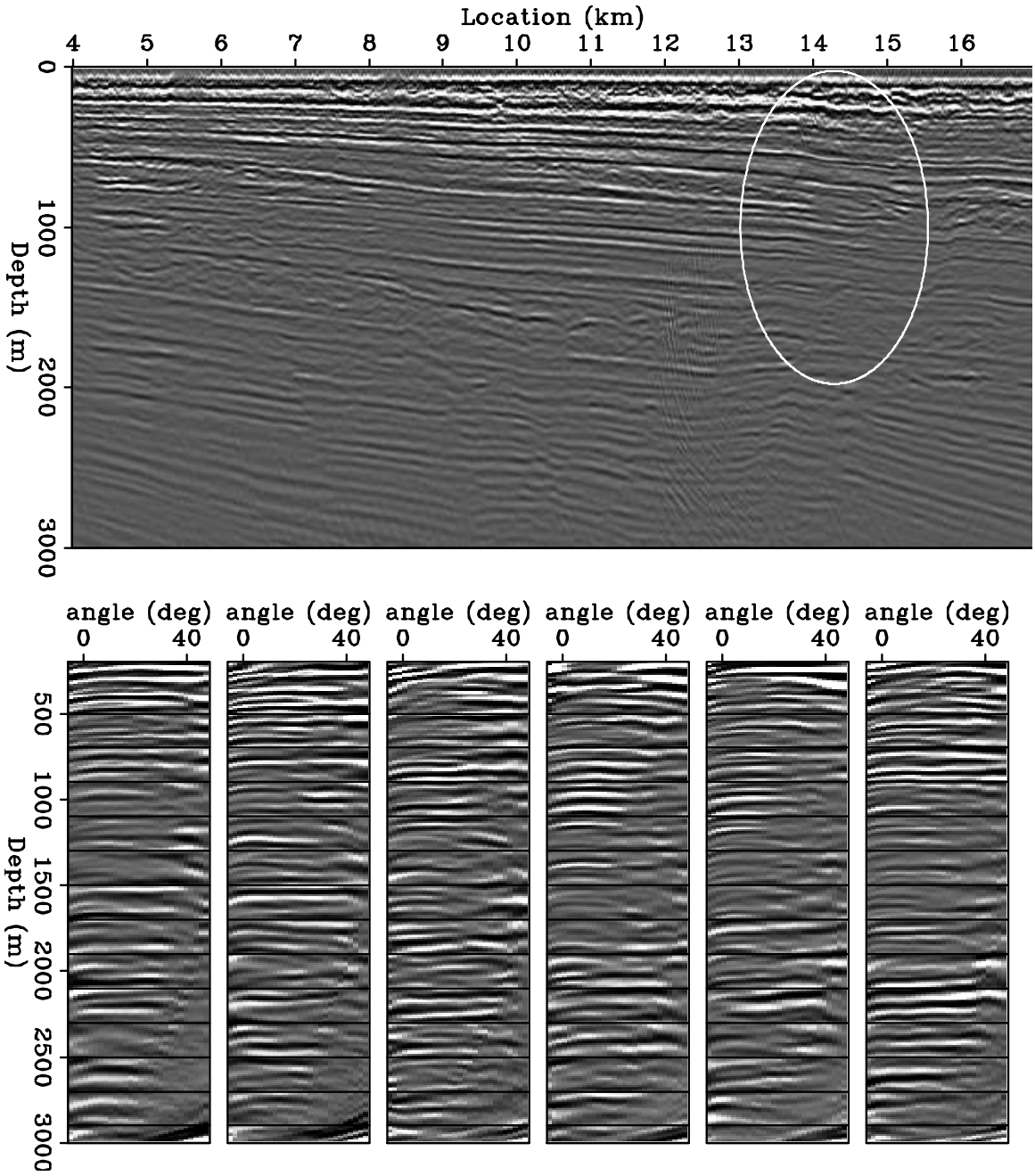

Figure 6: The initial stack image (Top panel) and initial angle domain common image gathers at CMP $= 7, 10, 13, 14, 14.5, 15$ km (Bottom row). [**CR**]

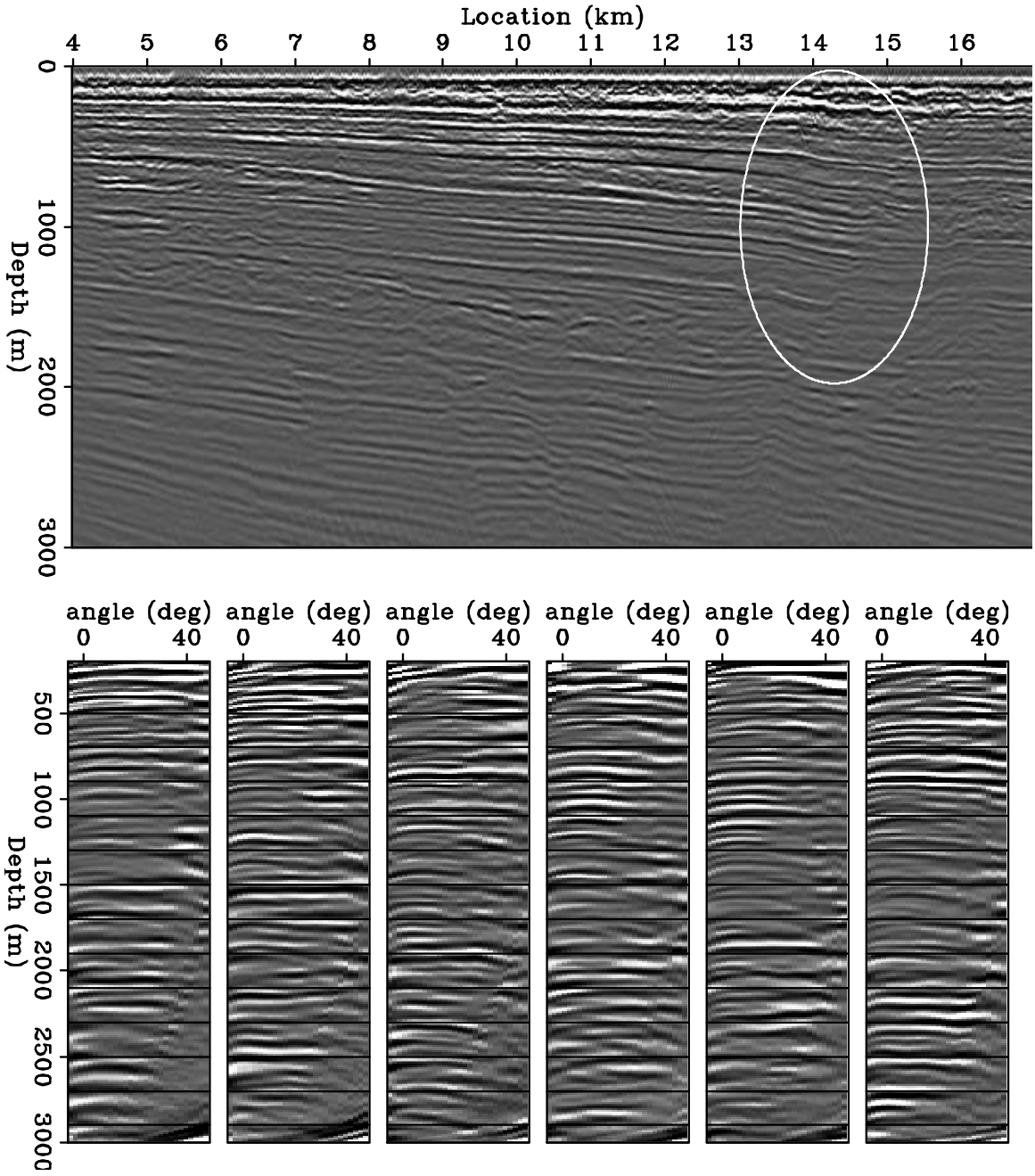

Figure 7: The final stack image (Top panel) and final angle domain common image gathers at CMP = $7, 10, 13, 14, 14.5, 15$ km (Bottom row). Compared with Figure 6, improvements in continuity and enhancements in amplitude strength are highlighted by the oval. [**CR**]

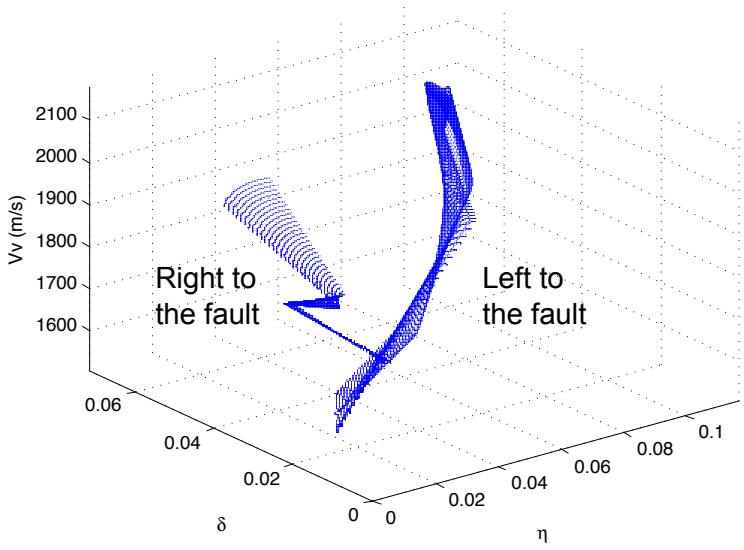

Figure 8: 3D scatter plot for the anisotropic parameters v_v, δ and η. [**CR**]

Sava, P. and S. Formel, 2006, Generalized imaging conditions for wave equation migration: CWP Report, **524**.

Shan, G., 2009, Optimized implicit finite-difference and fourier finite-difference migration for VTI media: Geophysics, WCA189–WCA197.

Shen, P., 2004, Wave-equation migration velocity analysis by differential semblance optimization: PhD thesis, Rice University.

Thomsen, L., 1986, Weak elastic anisotropy: Geophysics, **51**, 1954–1966.

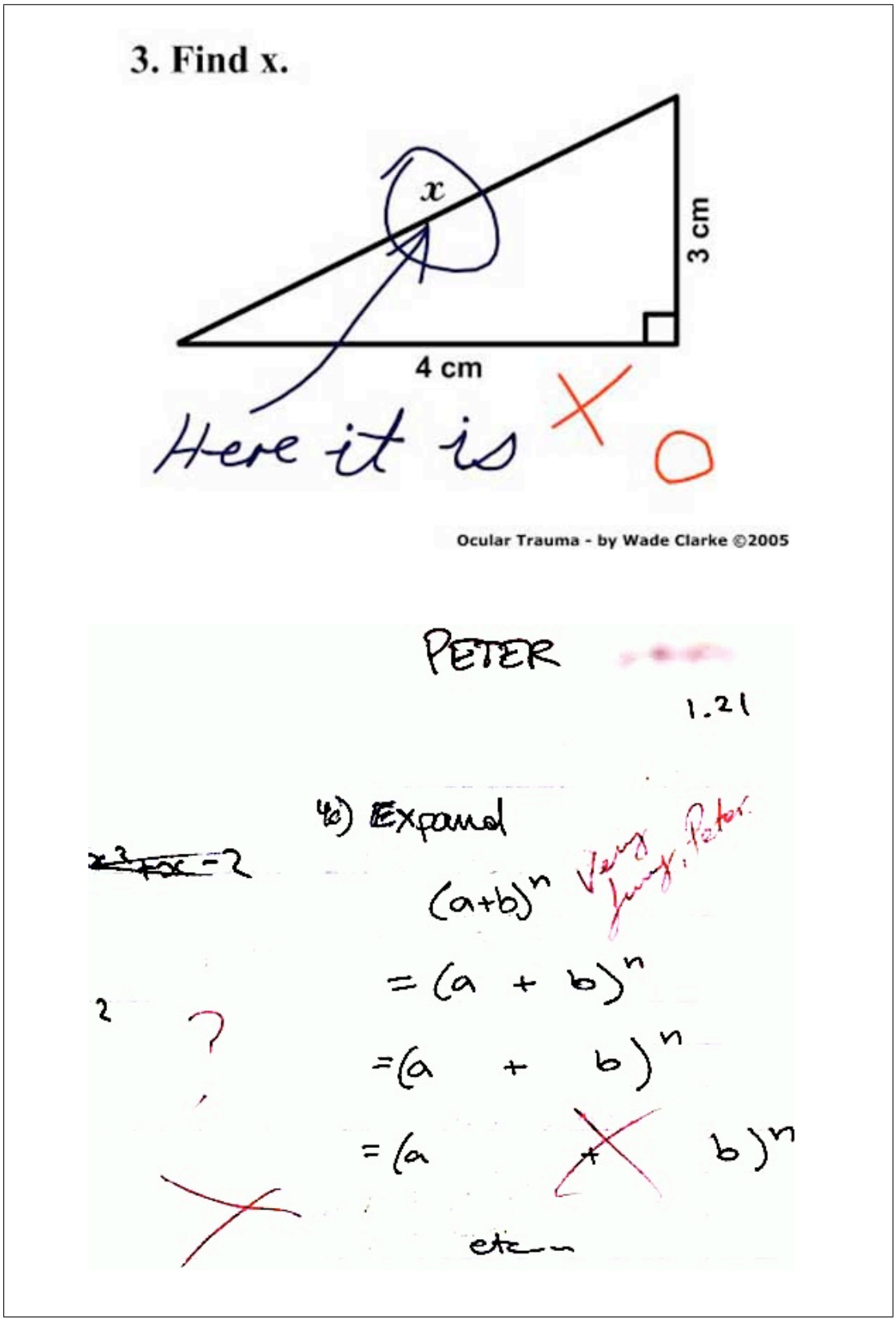
3. Find x.
x
3 cm
4 cm
Here it is
Ocular Trauma - by Wade Clarke ©2005
PETER
1.21
b) Expand
$(a+b)^n$
Very funny, Peter.
$= (a + b)^n$
$= (a + b)^n$
$= (a + b)^n$
etc...